Retrotransposons in Werner syndrome-derived macrophages trigger type I interferon-dependent inflammation in an atherosclerosis model

Sudip Paul
   Chiba University Graduate School of Medicine

Masamitsu Sone
   Chiba University Graduate School of Medicine

Ashwini Patil
   Combinatics Inc.

Hisaya Kato
   Chiba University Graduate School of Medicine

Yoshiro Maezawa
   Chiba University Graduate School of Medicine

Motohiko Oshima
   The Institute of Medical Science, The University of Tokyo

Masaki Fukuyo
   Chiba University Graduate School of Medicine

Bahityar Rahmutulla
   Chiba University Graduate School of Medicine

Yasuo Ouchi
   Salk Institute for Biological Studies

Kyoko Tsujimura
   Chiba University Graduate School of Medicine

Mahito Nakanishi
   TOKIWA-Bio, Inc.

Atsushi Kaneda
   Chiba University Graduate School of Medicine   https://orcid.org/0000-0002-6980-5515

Atsushi Iwama
   The Institute of Medical Science, The University of Tokyo   https://orcid.org/0000-0001-9410-8992

Koutaro Yokote
   Chiba University Graduate School of Medicine

Koji Eto
   Chiba University Graduate School of Medicine   https://orcid.org/0000-0002-5863-7122

Naoya Takayama（✉ tnaoya19760517@gmail.com ）

Article

Keywords:

Abstract

The underlying mechanisms of the second leading cause of death among Werner syndrome (WS) patients, atherosclerosis, is not fully understood. Here, we established an *in vitro* co-culture system using macrophages (iMφs), vascular endothelial cells (iVECs), and vascular smooth muscle cells (iVSMCs) derived from induced pluripotent stem cells. WS-iMφs induced endothelial dysfunction and characteristics of phenotype switching in WS-iVECs and WS-iVSMCs, respectively. RNA-seq and ATAC-seq revealed accelerated activation of type I interferon signaling and reduced chromatin accessibility of several transcriptional binding sites required for cellular homeostasis in WS-iMφs. Furthermore, we found higher expression of retrotransposable elements in WS-iMφs and WS peripheral blood-derived-Mφs and evidence that retrotransposable element-derived dsRNA may activate the *DHX58*-dependent cytoplasmic RNA sensing pathway in WS-iMφs. Conversely, silencing type I interferon signaling in WS-iMφs suppressed cellular senescence and inflammation. These findings suggest that Mφ-specific inhibition of type I interferon signaling could be targeted to treat atherosclerosis in WS patients.

Introduction

Vascular aging is a major risk factor for the onset of cardiovascular diseases, which are the leading cause of death worldwide [1,2,3]. Macrophages (Mφs) have long been known to contribute to inflammatory diseases including atherosclerosis. Mφs regulate local inflammation by secreting a wide array of pro-inflammatory cytokines and chemokines upon encountering various stimuli [4]. In particular, type I interferon (IFN) signaling under the regulation of IFN regulatory factor 3 (IRF3) and IRF7 transcription factors is a trigger of metabolic change, mitochondrial dysfunction, cellular senescence, and aging [5–8]. Growing evidence suggests that other than viral or foreign factors, cell-intrinsic factors such as reactive oxygen species (ROS), endoplasmic reticulum (ER) stress, DNA damage, and retrotransposable elements (RTEs) prime type I IFN-dependent immune responses [5,9–12].

RTEs, which include long-interspersed nuclear elements (LINEs), short-interspersed nuclear elements (SINEs), and endogenous retroviruses (ERVs), comprise up to half of the human genome and usually remain silent by maintaining repressive heterochromatin formation across the genome [13–15]. However, in some pathogenic conditions, RTEs are reactivated and have the potential to promote aberrant transcription (which may lead to inflammation), alternative splicing, insertional mutagenesis, DNA damage, and genome instability [16]. In addition, mechanisms that repress RTE activity become less efficient during the aging process [11,17]. Thus, RTEs were recently found to be associated with cancer, aging, and other cellular maintenance processes [11,17–19].

The *in vitro* generation of key players of atherosclerosis, including immune cells (e.g., Mφs) and vascular cells (e.g., vascular endothelial cells (VECs) and vascular smooth muscle cells (VSMCs)), from disease-specific human induced pluripotent stem cells (iPSCs) is a promising tool for mimicking compromised vessel walls [20]. Recently, we established disease-specific iPSCs from patients with Werner syndrome

(WS) [21], a rare human inherited disorder characterized by the appearance of premature aging induced by mutation of the *WRN* (RecQ Like Helicase) gene [22]. Atherosclerosis is frequently observed in WS patients and is their second leading cause of death after cancer [23,24]. Although a mouse model of WS does not recapitulate atherosclerosis [25]. In addition, WRN-deficient embryonic stem cells that are differentiated into endothelial cells do not show features of premature aging, however, a recent study reports that *in vitro* downregulation of *WRN* enhances the expression of factors that regulate cell adhesion and inflammation [26,27]. But this prior work did not consider that atherosclerosis develops from the orchestration of immune cells and vascular cells. Hence, the aim of this study was to generate, characterize, validate, and use immune and vascular cells differentiated from iPSCs from WS patients and age-matched healthy individuals and establish a novel *in vitro* model to better understand the atherosclerosis microenvironment at the molecular level.

Results

Differentiation and characterization of Mφs and vascular cells from human iPSCs

We modified the revised human pluripotent stem cell-derived sac (hPSC-sac) method [28–31] to generate functional Mφs (Extended Data Fig. 1a). Reverse transcription-quantitative polymerase chain reaction (RT-qPCR) analysis confirmed the mRNA expression of different Mφ maturation markers of iPSC-derived Mφs (iMφs) on day 21 of differentiation, whereas no such expression was detected in iPSCs or C3H10T1/2 feeder cells (Extended Data Fig. 2a). Also, iMφs on day 21 of differentiation expressed higher levels of Mφ maturation cell surface markers (e.g., CD16, CD14, CD11b, HLA-DR, CD68, CD80, CD163, and CD206) than hematopoietic progenitor cells (HPCs) on day 14 (Extended Data Fig. 2b). Giemsa-stained CD14$^+$CD11b$^+$ (FACS sorted) iMφs showed circular or irregular shapes with rich cytoplasm and a large nucleus (Extended Data Fig. 2c). Next, we performed phagocytosis assay,[32] and confirmed the significant phagocytosis activity of iMφs (Extended Data Fig. 2d). In addition, when we treated iMφs with lipopolysaccharide (LPS) and assessed their immune response, we found dose-dependent mRNA expression of pro-inflammatory cytokines (Extended Data Fig. 2e).

We also used the hPSC-sac method to generate vascular progenitor cells (VPCs) on growth-arrested C3H10T1/2 feeder cells. These VPCs were further directed to differentiate into VECs or VSMCs in the presence or absence of vascular endothelial growth factor (VEGF), respectively (Extended Data Fig. 1b,c). After seven day-differentiation from VPCs, iPSC-derived VECs (iVECs) positive for VE-cadherin (CD144), CD34, and CD31 were induced (Extended Data Fig. 2f). We observed VEC-like morphologies (Extended Data Fig. 2g) and confirmed that iVECs expressed common markers of VECs (i.e., von Willebrand factor (vWF), VE-cad, eNOS, and CD31) at similar levels as human aortic endothelial cells (HAEC) (Extended Data Fig. 2h). In addition, immunocytochemistry confirmed that iVECs expressed VE-cadherin (Extended Data Fig. 2i) and exhibited uptake of acetylated low-density lipoprotein (Extended Data Fig. 2j). As for iPSC-derived VSMCs (iVSMCs), they had VSMC-like morphologies (Extended Data Fig. 2k) and showed protein (Extended Data Fig. 2l) and gene (Extended Data Fig. 2m) expression of VSMC maturation

markers. Collectively, these results indicate the successful induction of functional human iMφs, iVECs, and iVSMCs.

Apoptosis and cellular senescence-dependent impaired cell proliferation capacity of WS-iMφs

We next investigated differences in induction efficiency, cell proliferation, and oxidized low-density lipoprotein (oxLDL) uptake between healthy- and WS-iMφs, iVECs, and iVSMCs. No notable differences were observed between HPC and VPC generation or between iVEC and iVSMC proliferation (Extended Data Fig. 3a-c). Moreover, we observed no difference in oxLDL uptake or foam cell formation between WS- and healthy-iMφs (Extended Data Fig. 3d,e). However, WS-iMφs showed significantly lower proliferation capacity than healthy-iMφs (Fig. 1a). When we assessed whether the low proliferation of WS-iMφs was due to apoptotic cell death or cellular senescence before or after oxLDL treatment, we found that the proportion of annexin V$^+$ cells was significantly higher among WS-iMφs (13.0%) than among healthy-iMφs (4.6%) (Fig. 1b). In addition, mRNA expression of the vital cell cycle inhibitor *CDKN1A*, which is strongly correlated with apoptotic cell death, was significantly higher in WS-iMφs than in healthy-iMφs (Fig. 1c), suggesting the increased apoptosis in WS-iMφs.

We further performed senescence assay using fluorescently labeled senescence-associated beta-galactosidase (SA-β-gal) in healthy- and WS-iMφs. The mean fluorescence intensity (MFI) of SA-β-gal was significantly higher for WS-iMφs than for healthy-iMφs irrespective of oxLDL treatment (Fig. 1d). Consistently, mRNA expression of the senescence-associated gene *CDKN2A* was significantly higher in WS-iMφs than in healthy-iMφs irrespective of oxLDL treatment (Fig. 1e). Furthermore, in line with previous findings that senescent cells secrete a wide array of pro-inflammatory cytokines, WS-iMφs showed secretion of pro-inflammatory cytokines including interleukin (IL)-6, IL-1β, and tumor necrosis factor-alpha (TNFα) after oxLDL treatment (Fig. 1f).

Recapitulation of early-stage atherosclerosis by co-culture of iMφs and iVECs or iVSMCs

Interactions among VECs, VSMCs, and the immune system play a vital role in the progression and outcome of cardiovascular diseases and atherosclerosis [33]. Therefore, to assess the effect of inflammatory iMφs on iVECs and iVSMCs *in vitro,* we co-cultured healthy- and WS-iMφs with healthy- and WS-iVECs or iVSMCs (Extended Data Fig. 4a).

Endothelial dysfunction is a hallmark of early-stage atherosclerosis and is characterized by increased Mφ adhesion, inflammation, and extracellular matrix degradation (Extended Data Fig. 4b). VEC-Mφ adhesion may be the initial stage of atherosclerotic plaque formation [34]. Accordingly, significantly more adherent Mφs were found in the WS group than in the healthy group (Fig. 2a). Next, we found significantly higher pro-inflammatory cytokine (IL6 and TNF-α) and matrix metalloproteinase-1 protein (MMP1) secretion and

mRNA expression in WS-iVECs than in healthy-iVECs when co-cultured with inflammatory Mφs (Fig. 2b). Thus, in our co-culture system, WS-iVECs recapitulated all the aforementioned phenotypes, suggesting that they are more vulnerable to endothelial dysfunction than healthy-iVECs.

Next, we assessed the effect of iMφ co-culture on iVSMCs. The historical view of VSMCs in atherosclerosis is that 'aberrant' proliferation of VSMCs promotes plaque formation [35]. The switching of VSMCs from a contractile phenotype to an adverse synthetic phenotype is a hallmark of atherosclerosis, which begins with high VSMC proliferation and reduced expression of VSMC contractile markers (Extended Data Fig. 4c) [36]. Accordingly, we found that WS-iVSMCs were more highly proliferative than healthy-iVSMCs when co-cultured with inflammatory Mφs (Fig. 2c). Meanwhile, although we observed steady-state mRNA expression of VSMC markers in both healthy- and WS-iVSMCs at similar levels, co-culture with inflammatory Mφs reduced mRNA levels of the VSMC markers *CNN1*, *ACTA2*, *TAGLN,* and *SMTN* in WS-iVSMCs but not in healthy-iVSMCs (Fig. 2d). In addition, immunocytochemistry analysis revealed that calponin-1 protein decreased in WS-iVSMCs co-cultured with inflammatory Mφs, whereas this phenomenon was not observed in healthy-iVSMCs (Fig. 2e). Taken together, these results suggest that WS-iVSMCs are more prone to switching from a contractile phenotype to a more rigid synthetic phenotype.

Upregulated type I IFN signaling pathway in WS-iMφs as revealed by RNA-seq analysis

To characterize the phenotype of WS-iMφs in more detail, we performed RNA-sequencing (RNA-seq) analysis in healthy- and WS-iMφs with or without oxLDL treatment (Fig. 3a). A heatmap shows 3,536 differentially expressed genes derived from Cuffdiff analysis grouped in four clusters based on k-means clustering (Fig. 3b,c). We next performed pathway enrichment analysis of individual gene sets within each cluster. As expected from the finding that healthy-iMφs showed less apoptosis and senescence than WS-iMφs (Fig. 1b-e), cell cycle and DNA repair-related pathway genes were enriched only in cluster 1, which was highly expressed in healthy-iMφs without oxLDL treatment (Fig. 3d,e).

Regarding cluster 2, which was highly expressed in healthy-iMφs treated with oxLDL, pathway enrichment analysis showed enrichment of stress-responsive pathways (Extended Data Fig. 5a). In addition, mRNA levels of the transcription factor nuclear factor erythroid 2-related factor 2 (*NRF2*), encoded by the *NFE2L2* gene that regulates expression of antioxidant proteins [37,38], and other vital antioxidative enzymes increased significantly after treatment with oxLDL in healthy-iMφs but not in WS-iMφs (Extended Data Fig. 5b). These genes function as antioxidants by reducing oxidative agents, thereby protecting cells from oxidative damage. Collectively, these results suggest that WS-iMφs fail to generate sufficient levels of antioxidants and thus have a higher burden of oxidative stress after oxLDL treatment.

Regarding cluster 4, which was highly expressed in WS-iMφs treated with oxLDL, pathway enrichment analysis showed enrichment of immune system, and innate immunity, related pathways (Fig. 3f). In particular, higher expression was observed for type I IFN signature-related genes, whereas few of these

genes were upregulated before oxLDL treatment in WS-iMφs (Fig. 3g), suggesting predominant upregulation of endogenous type I IFN signals in WS-iMφs. Apoptotic cell-related gene sets were also enriched in cluster 4 (Fig. 3h).

Type I IFN-specific chromatin accessibility profile of WS-iMφs

To better understand WS-related epigenetic remodeling in iMφs, we performed open chromatin analysis via transposase-accessible chromatin using sequencing (ATAC-seq) [39,40]. Principal component analysis showed that healthy- and WS-iMφs exhibited separate clustering, but there was no clear separation between WS-iMφs with and without oxLDL treatment (Fig. 4a). Next, we compared differentially accessible regions (DARs) between healthy- and WS-iMφs regardless of oxLDL treatment. The heatmap shows a total of 1,761 differentially open chromatin sites, with only 134 open sites observed in WS-iMφ groups (Fig. 4b). As a previous study reports a global reduction in chromatin accessibility in senescence-related macular degeneration [41], we speculated that a Mφ-specific reduction in chromatin accessibility is associated with cellular senescence. To identify differences in chromatin accessibility among samples, we applied non-negative matrix factorization (NMF) to the signal over background at each peak identified in any sample. We found differences between healthy- and WS-iMφ NMF signatures regardless of oxLDL treatment (Fig. 4c). To identify the key molecules in each signature, we performed motif enrichment analysis using HOMER. We found that IRF, CEBP, FOSL2, ATF, and AP-1 motifs were enriched in WS-iMφs, whereas the binding sites of several important transcription factors (e.g., GATA, E2F, OCT, CTCF, TCF, and PAX) were closed in WS-iMφs (Fig. 4d-f). These findings suggest that aging, but not oxLDL treatment, closed many regions that are necessary for proper cellular homeostasis and opened regions that could cause inflammation in WS-iMφs.

Inhibition of cell proliferation and promotion of cellular senescence by type I IFN signaling in WS-iMφs

To investigate the effects of type I IFN signaling on WS-iMφs, we knocked down IRF3 and IRF7 (IRF3/7), which are key transcription factors that contribute to the transcriptional activation of virus-inducible cellular genes including type I IFN genes, using a lentiviral shRNA system [42]. As type I IFN signature genes were upregulated only in WS-iMφs, we investigated the effects of IRF3/7 KD in this cell type. shRNA-mediated knockdown significantly reduced mRNA levels of *IRF3/7* (Fig. 5a). In accordance with the known induction of the transcription of several type I IFN signature genes including *ISG15*, *MX1*, and *MX2* by IRF3/7, mRNA levels of *ISG15*, *MX1*, and *MX2* were suppressed after *IRF3/7* knock down compared with after control shRNA transduction in WS-iMφs (Fig. 5b). Next, we investigated the effects of IRF3/7 knock-down on cell proliferation and cellular senescence. We found that WS-iMφs exhibited higher proliferation (Fig. 5c) and reduced expression of SA-β-gal (Fig. 5d) and *CDKN2A* mRNA after IRF3/7 knock down than after control shRNA transduction (Fig. 5e). Furthermore, the secretion and mRNA expression of pro-inflammatory cytokines *IL6* and *TNF-α* were significantly reduced after IRF3/7 knock

down (Fig. 5f,g). Collectively, these results suggest that type I IFN signaling promotes the senescence-associated inflammatory response and, conversely, that silencing the expression of *IRF3/7* suppress senescence and inflammation in WS-iMφs.

The resurrection of retrotransposons in WS-iMφ activated the innate immune system via DHX-58-dependent manner

As our culture system did not contain the virus or IFN itself, we speculated that type I IFN signaling is upregulated by a cell-intrinsic mechanism. To identify the trigger of type I IFN signaling in WS-iMφs, we examined factors (i.e., ROS, ER stress, DNA damage, and RTEs) that could potentially induce a type I IFN response other than viral infection [5,9–12]. WS-iMφs showed increased accumulation of cellular ROS and higher mRNA expression of the ROS generator NADPH oxidase 2 (*NOX2*) (Extended Data Fig. 6a,b) [43]. Although *NOX2* inhibition in WS-iMφs significantly reduced ROS generation (Extended Data Fig. 6c), we found no notable association of type I IFN signature genes with ROS in WS-iMφs (Extended Data Fig. 6d).

Next, we investigated whether ER stress initiated the type I IFN response in WS-iMφs by examining the mRNA expression of ER stress-related genes (i.e., *ATF6, PERK, CHOP,* and *IRE1*) but observed no notable changes (Extended Data Fig. 7a). Furthermore, the cGAS−STING signaling pathway, a sensor of cytosolic DNA, was recently found to be a key mediator of the type I IFN response and is implicated in many inflammatory diseases[44]. However, there were no significant differences in the mRNA expression of cGAS and STING genes between healthy- and WS-iMφs except for STING gene treated with oxLDL (Extended Data Fig. 7b). For further confirmation, we blocked the reverse transcription of RNA to DNA using two nucleoside/nucleotide reverse transcriptase inhibitors, lamivudine and emtricitabine, but observed no notable changes in the expression of cGAS, STING, or type I IFN signature genes (Extended Data Fig. 7c-e).

Finally, we analyzed the expression of RTEs in healthy- and WS-iMφs with or without oxLDL treatment and in peripheral blood-derived primary Mφs (PB-Mφs) from healthy aged and WS patients. To systematically examine global RTE expression in iMφs and PB-Mφs, we used RNA-seq analysis. We identified the genomic regions representing RTEs and used the RNA read counts within these regions in each sample to identify differentially expressed RTEs. Heatmaps of iMφs and PB-Mφs showed similar upregulation of RTE expression in WS-derived cells compared with healthy cells regardless of oxLDL treatment. A total of 148, 176, and 205 RTEs were significantly upregulated in untreated WS-iMφs, WS-iMφs treated with oxLDL, and WS-PB-Mφ, respectively. By contrast, only 20, 23, and 34 RTEs were upregulated in untreated healthy-iMφs, healthy-iMφs treated with oxLDL, and healthy-PB-Mφs, respectively (Fig. 6a). All RTE families—LINE, SINE, and ERV—were significantly upregulated in WS cells (Fig. 6b-d).

To evaluate the commonality of gene expression of RTEs in WS-iMφs and WS-PB-Mφs, we aggregated individual RTEs at the sub-family level. We found that 43 RTE sub-families were upregulated in both cell types (Fig. 6e). In addition, we confirmed that aging- or cancer-associated RTEs (e.g., L1M5, L2b, MIRb, AluJr, MLT1A0, and MER5A) were upregulated in both WS-iMφs and WS-PB-Mφs (Fig. 6f-h) [18,45–49].

Viral double-stranded (ds)RNA is readily sensed by RIG-I-like receptors and *IFIH1*, leading to the propagation of signals to the nucleus via mitochondrial antiviral-signaling protein (MAVS) and ultimately initiation of the type I IFN response (Fig. 7a) [50]. RTEs are usually generated in the nucleus and released into the cytoplasm, where they form double-stranded RNA (dsRNA) that is detected by cytosolic RNA sensors and evokes the type I IFN response, which is called viral mimicry [51,52]. When we stained cells with anti-dsRNA antibody, we found that WS-iMφs accumulated ~2.5 times more dsRNA than healthy-iMφs (Fig. 7b). We also confirmed that *IFIH1* and *DHX58* were upregulated in WS-iMφs (Fig. 3g). Furthermore, flow cytometry showed that MAVS was highly activated in WS-iMφs (Fig. 7c), suggesting the activation of this pathway.

To determine whether dsRNA induces type I IFN signaling through cytosolic RNA sensors, we suppressed a significantly enriched nucleic acid sensor in this pathway, *DHX58*, in WS-iMφs (Fig. 7d). We found that the expression of the several type I IFN signature genes, including *IRF7*, *ISG15*, *MX1*, and *MX2*, which are downstream targets of the *DHX58* gene, were downregulated in *DHX58* knock-down cells (Fig. 7e). Taken together, these results suggest that RTE-derived dsRNA is detected by *DHX58* and initiates the transcription of type I IFN signature genes.

Discussion

This study describes an efficient technique for investigating vascular aging and human pathologies affecting the cardiovascular system in WS through the direct differentiation of iPSCs into human myeloid and vascular cells. Using these cells, we successfully established an *in vitro* 2D co-culture system to study atherosclerosis at the molecular level. Regardless of oxLDL treatment, RNA-seq and ATAC-seq revealed accelerated activation of type I IFN signaling and reduced chromatin accessibility of several transcription factors essential for cellular homeostasis in WS-iMφs, which are culprits for aberrant inflammation and cellular senescence. Furthermore, we showed that activation of RTEs led to the release of dsRNA into the cytosol, which in turn activated the *DHX58*-dependent nucleic sensing pathway followed by type I IFN signaling in WS-iMφs, resulting in aberrant inflammation and cellular senescence. These results suggest that WS cells themselves become a risk factor for chronic inflammation and atherosclerosis, independent of the high blood glucose or hyperlipidemia frequently observed in WS patients.

 Type I IFN signaling was recently recognized as an inducer of atherosclerosis. Type I IFN signaling is upregulated by viral infections or exposure to single- or double-stranded nucleic acids via toll-like receptors, cGAS-STING or RIG-I-like receptor-dependent pathways, and some growth factors and cytokines [53]. Toll-like receptors are cell surface receptors that play crucial roles in identifying extracellular

pathogens including viral RNA [54]. On the other hand, RIG-I-like receptors (e.g., *DDX58*, *DHX58*, and *IFIH1*) detect single-stranded RNA and dsRNA that accumulates in the cytoplasm and evokes type I IFN responses in a *IRF3/7*-dependent manner [51]. Surprisingly, we found upregulation of type I IFN signaling in WS-iMφs even though the culture medium did not contain any pathogens or IFN-α/β cytokines. We did not observe associations among ROS, ER stress, or DNA sensing via the cGAS-STING pathway with the expression of type I IFN genes (Extended Data Fig. 6,7). These results suggest that the RTE-RIG-I-like receptor pathway induced type I IFN signaling, leading to cellular senescence and proliferation arrest in WS-iMφs [5,55,56].

The RTE-dependent type I IFN response is well studied in both mouse models and human cells [11,57]. Recent reports suggest that RTE-derived dsRNA activates RIG-I-like receptor-dependent IFN responses in several types of cancer [51,58]. We demonstrated that 43 RTE families were commonly upregulated in iMφs and PB-Mφs, including aging- and cancer-associated RTEs [18,45–48]. A recent study demonstrates that reactivation of LINE1 (L1) elements causes cytoplasmic accumulation of L1 cDNA and promotes aging-associated inflammation by activating the type I IFN response. Conversely, inhibiting L1 replication improves the health and lifespan of aged mice [17]. In addition to L1, suppression of SINE Alu elements reverses the senescence phenotype, thus restoring cell self-renewal properties [18]. Furthermore, ERVs are linked to the induction of growth-inhibiting immune responses. DNA methyltransferase inhibitors upregulate ERVs, triggering cytosolic sensing of dsRNA that results in a type I IFN-dependent immune response and apoptotic cell death [12,19,51]. Hence, aberrant RTE expression is associated with inflammation and cellular aging/apoptosis.

In conclusion, to our knowledge, this is the first study showing clear evidence that aberrant RTE expression and upregulation of IFN signaling in Mφs contributes to atherosclerosis development. WS-iMφs in a pro-inflammatory state are the main malefactors that prime the development of and drive atherosclerosis progression in WS patients independent of diabetes mellitus and hyperlipidemia. Conversely, silencing type I IFN signaling attenuated WS-iMφ senescence and inflammation. Taken together, the results of our study indicate that targeting type I IFN signaling may be an attractive way of preventing and treating atherosclerosis in WS patients.

Materials And Methods

Cell culture

We recently established healthy and WS patient-derived iPSCs [21]. In this study all the experiments, except Fig. 4 and 6, were performed using three individual iPSC clones obtained from three different WS patients and three different age-matched healthy donors. In Fig. 4 and 6, we used two different iPSC clones from WS patients and age-matched healthy donors. On every passage, sub-confluent iPSCs were treated with 0.05% trypsin-EDTA (cat. #32778-34, Nacalai Tesque) at 37°C for 5-6 min and suspended with 1 ml Dulbecco's Modified Eagle's Medium (DMEM; cat. #08459-64, Nacalai Tesque) with 10% fetal bovine

serum (FBS; cat. #FB-1365/500, Biosera) by gentle pipetting. Single cells were plated on newly prepared Matrigel (cat. #356230, Corning)-coated 6-cm plates at 2.5-3 × 10^3/cm^2 with AK02N (ANJINOMOTO) supplemented with 1 μM Y-27632 (cat. #036-24023, Fujifilm). After 24 h, the culture medium was changed to medium without Y-27632. C3H10T1/2 cells were obtained and cultured as previously described [29]. Human aortic endothelial cells obtained from Lonza (CC-2535), and human aortic smooth muscle cells obtained from Gibco (C0075C) were cultured according to the manufacturers' protocols. All studies were performed in accordance with the Declaration of Helsinki. The ethics committee of Chiba University, Chiba, Japan (#1145) approved this study.

Differentiation of Mφs from iPSCs

We previously demonstrated that multipotent HPCs can be efficiently generated from human embryonic stem cells and iPSCs [28–31]. Here, we modified the PS-sac method to generate functional Mφs (Extended Data Fig. 1a). To obtain HPCs, PS-sac-like structures in culture were maintained for 2 weeks to obtain CD34$^+$ CD43$^+$ cells, followed by an additional 7 days of culture with a cytokine cocktail supported by growth-arrested C3H10T1/2 feeder cells (Extended Data Fig. 1a). Briefly, iPSCs were dissociated into small colonies (< 100 cells) with the aid of CTK (phosphate buffered saline (PBS) containing 0.25% trypsin (cat. #15090-046, Gibco), 1 mM CaCl$_2$, and 20% knock-out serum replacement (KSR; cat. #10828028, Gibco)) and cultured on a C3H10T1/2 feeder layer in differentiation medium (Iscove modified Dulbecco medium (IMDM) supplemented with a cocktail of 10 μg/mL human insulin, 5.5 μg/mL human transferrin, 5 ng/mL sodium selenite, 2 mM L-glutamine, 0.45 mM-monothioglycerol, 50 g/mL ascorbic acid, 15% highly filtered FBS) supplemented with 20 ng/mL recombinant human VEGF (R&D Systems) and 10 ng/mL human BMP4 (cat. #314-BP/CF-500, R&D Systems) in a low O$_2$ (5%) incubator at 37°C. On day 4, the differentiation medium was changed to medium supplemented with 20 ng/mL recombinant human VEGF, 50 ng/mL human bFGF (cat. #064-04541, Fujifilm), 10 μM SB431542 (cat. #192-16541, Fujifilm), and 10 U/mL heparin (cat. #873334, Awai Pharma Co., Ltd.) and kept under low O$_2$. On day 7, the differentiation medium was changed to medium without human bFGF and SB431542 (but including the other two factors at the same concentrations) and cultured in an atmospheric (20%) O$_2$ incubator. Finally, on day 10, the medium was changed to medium without heparin (but including recombinant human VEGF at the same concentration). On days 14-15, PS-sacs were trypsinized with 2.5% trypsin-EDTA (cat. #209-16941, Fujifilm), gently crushed by pipetting, and passed through a 40-μm cell strainer. Cells were then spun down, resuspended in staining medium (2% FBS in PBS), and stained with anti-CD34 (cat. #343508, Biolegend) and anti-CD43 (cat. #343206, Biolegend) antibodies. FACS-sorted CD34$^+$ CD43$^+$ HPCs were cultured on a fresh C3H10T1/2 feeder layer in 24- or 96-well culture plates at a density of 1 × 10^5 cells/well for 24-well plates and 5 × 10^4 cells/well for 96-well plates and maintained in differentiation medium supplemented with 25 ng/mL SCF, 5 ng/mL TPO, 50 ng/mL M-CSF, 50 ng/mL GM-CSF, 25 ng/mL G-CSF, and 25 ng/mL IL-3 (all from R&D Systems).

Differentiation of vascular cells from iPSCs

iPSC-derived vascular cells were induced using a modified version of a previously established protocol [59,60]. To generate VPCs, we took advantage of the previously established embryonic stem-sac method [28-31]. iPSCs were dissociated into small colonies (< 100 cells) with the aid of CTK (PBS containing 0.25% trypsin, 1 mM $CaCl_2$, and 20% KSR) and cultured on a C3H10T1/2 feeder layer in differentiation medium supplemented with 20 ng/mL recombinant human VEGF in an incubator at 37°C. The culture medium was changed with fresh medium every 3 days. On days 10-11, PS-sacs were trypsinized with 2.5% trypsin-EDTA, gently crushed by pipetting, and passed through a 40-μm cell strainer. Cells were then spun down, resuspended in staining medium, and stained with CD34 (cat. #343508, Biolegend), VEGF-R2 (CD309; cat. #359912, Biolegend), and TRA 1-60 (cat. #560173, BD Pharmingen) antibodies. FACS-sorted cells were seeded (CD34$^+$ cells for VEC induction and CD34$^-$ VEGF-R2$^+$ cells for VSMC induction) on a C3H10T1/2 feeder layer at a density of 1.5×10^4 cells/cm^2 on a 24-well plate and maintained in differentiation medium supplemented with 10% FBS with (for VECs) or without (for VSMCs) 100 ng/mL recombinant human VEGF.

Differentiation of monocytes/macrophages from human peripheral blood derived mononuclear cells.

Peripheral blood from healthy donors and WS patients were obtained and purified to mononuclear cells according to our previous study [21]. Peripheral blood-derived CD34 negative mononuclear cells were then stained with anti-CD33, anti-CD43, anti-CD14, and anti-CD11b antibodies followed by incubation for 30 min on ice in the dark, washed with cold staining medium, and sorted CD33$^+$CD43$^+$CD14$^+$CD11b$^+$ monocytes/macrophages using a BD FACSAria IIIu system (Becton Dickinson Japan, Tokyo, Japan).

Cell sorting and flow cytometric analyses

Cells were suspended in staining medium, incubated for 30 min with appropriate antibodies on ice in the dark, washed with cold staining medium, and sorted or analyzed using a BD FACSAria IIIu system (Becton Dickinson Japan, Tokyo, Japan) or BD FACS Canto II cytometer (Becton Dickinson Japan, Tokyo, Japan).

Giemsa staining

On day 21 of differentiation, iMφs were stained with Hemacolor (cat. #111661, Merec) according to the manufacturer's protocol. Stained cells were air-dried and observed using a microscope (Nikon Eclipse Ts2R, Japan).

RT-qPCR

Total RNA was extracted using a RNeasy Micro Kit (cat. #74034, Qiagen, Hilden, Germany) and reverse-transcribed using SuperScript VILO™ Master Mix (cat. #11755250, Thermo Fisher Scientific, Waltham, MA). Primer sets were designed by our laboratory or purchased from Thermo Fisher Scientific. Quantitative real time PCR was carried out with SYBR™ Green PCR Master Mix (cat. #4472908, Applied

Biosystems) using a Bio-Rad CFX real-time PCR system. Gene expression was analyzed relative to that of *GAPDH*.

Immunocytochemistry

For detection of intracellular proteins, vascular cells were cultured in four-well slide chambers (cat. #SCS-N04, Matsunami). On days 17-18 of differentiation, VECs or VSMCs were washed twice with PBS and fixed with 4% paraformaldehyde (cat. #161-20141, Fujifilm) in PBS for 10 min at room temperature. Cells were then washed three times with PBS and permeabilized with 0.1% Triton X100 (cat. #35501-15, Nacalai Tesque) and 10% FBS (Biosera) in PBS for 30-40 min, followed by blocking for at least 1 h at room temperature with Blocking One (cat. #03953-66, Nacalai Tesque). Blocked cells were incubated with primary antibodies diluted in blocking solution at 4°C overnight on a rotator. On the following day, after three washes with PBS, appropriate fluorescence-labeled secondary antibodies were added and incubated at room temperature for at least 1 h in the dark, after which cells were washed thoroughly with PBS and mounted on microscope slides using ProLong™ Diamond Antifade Mountant with DAPI (cat. #P36962, Invitrogen, Carlsbad, CA). Slides were allowed to air-dry before examination using a fluorescence microscopy (Nikon), and images were merged using Adobe Photoshop software. Primary antibodies were anti-α-SMA (1:1,000, cat. #ab7817, Abcam, Cambridge, UK), anti-calponin-1 (1:500, cat. #abt129, Merck-Millipore, Darmstadt, Germany), and anti-VE cadherin (1:500, cat. #ab33168, Abcam). Secondary antibodies were goat anti-mouse IgG H&L (cat. #ab150113, Abcam) and goat anti-rabbit IgG H&L (cat. #ab150078, Abcam).

oxLDL and acetylated low-density lipoprotein uptake assay

iMφs were serum-starved for 24-36 h in Iscove's Modified Dulbecco's Medium (IMDM) supplemented with 1% bovine serum albumin (BSA) on day 20 of differentiation. oxLDL labeled with 1, 1'-dioctadecyl-3,3',3'-tetramethylindocarbocyanine (DiI; cat. #L34358, Invitrogen) was added to cells at a concentration of 50 µg/mL with IMDM containing 1% BSA and incubated for 5-6 h in a 37°C incubator.

iVECs and human aortic endothelial cells were serum-starved for 24-36 h in IMDM supplemented with 1% BSA on day 16 of differentiation (in the case of iVECs). Acetylated low-density lipoprotein labeled with DiI (cat. #BT-902, Alfa Aesar) was added to cells at a concentration of 50 µg/mL with IMDM containing 1% BSA and incubated for 5-6 h in a 37°C incubator.

Apoptosis assay by flow cytometry

On day 20 of differentiation, healthy- and WS-iMφs were serum-starved for 24-36 h, incubated for 5-6 h with DiI-oxLDL at a concentration of 50 µg/mL, and washed three times with PBS. Apoptosis assay was performed for untreated and oxLDL-treated iMφs using the FITC Annexin V detection kit (cat. #556547, BD Pharmingen) according to the manufacturer's protocol and analyzed with a FACS CantoII cytometer (BD).

Senescence assay by flow cytometry

On day 20 of differentiation, healthy- and WS-iMφs were serum-starved for 24-36 h, incubated for 5-6 h with DiI-oxLDL at a concentration of 50 μg/mL, and washed three times with PBS. Senescent SA-β-gal^{+} cells were then detected among untreated and oxLDL-treated iMφs using the Cellular Senescence Flow Cytometry Assay Kit (cat. #CBA-232, Cell Biolabs, Inc.) according to the manufacturer's protocol and analyzed with a FACS CantoII cytometer (BD).

Coculture of iMφs with iPSC-induced vascular cells

On day 20 of differentiation, iMφs were serum-starved for 24-36 h and incubated for 5-6 h with DiI-oxLDL at a concentration of 50 μg/mL. After washing three times with PBS, untreated or oxLDL-treated 7×10^4 iMφs (on a 24-well plate) were seeded onto iPSC-derived mature vascular cells (on day 17) and maintained with iMφ differentiation medium for 72 h until further analysis. Cell culture supernatant was collected and filtered with a 0.22-μm filter followed by ELISA to assess protein levels. Cells were then trypsinized with 0.05% trypsin-EDTA (Gibco), gently crushed by pipetting, spun down and resuspended in staining medium, and stained with CD14 (cat. #A22331, Backman Counter) for 30 min on ice in the dark. CD14^{-} iPSC-derived vascular cells were then sorted for RT-qPCR gene expression analysis.

Mφ-VEC adhesion assay

On day 20 of differentiation, iMφs were serum-starved for 24-36 h and incubated for 6 h with DiI-oxLDL at a concentration of 50 μg/mL. After washing three times with PBS, untreated or oxLDL-treated 7×10^4 iMφs were seeded onto iPSC-derived mature vascular cells on day 17 and maintained with iMφ differentiation medium for 72 h until further analysis. Cells were gently washed with PBS three times, trypsinized with 0.05% trypsin-EDTA (Gibco), gently crushed by pipetting, spun down and resuspended in staining medium, and stained with CD14 for 30 min on ice in the dark. CD14^{+} Mφs were then counted with CountBright (cat. #C36950, Invitrogen) using a BD FACSAria IIIu system.

RNA-seq and analysis

On day 20 of differentiation, iMφs were serum-starved for 24-36 h and incubated for 6 h with DiI-oxLDL at a concentration of 50 μg/mL. Cells were then washed three times with PBS, suspended in staining medium, incubated for 30 min with anti-CD14 and anti-CD11b antibodies (cat. #301318, Biolegend) on ice, and washed with cold staining medium. oxLDL^{+} CD14^{+} CD11b^{+} cells were sorted into Buffer RLT Plus. Total RNA from untreated or oxLDL-treated healthy- and WS-iMφs was isolated using an RNeasy Micro Kit (QIAGEN). RNA-seq libraries were prepared from at least three biological replicates according to the manufacturer's protocol. Briefly, ~10 ng total RNA was used as input for cDNA conversion using a SMART-Seq v4 Ultra Low Input RNA Kit for Sequencing (cat. #634890, Clontech, Takara). cDNA was fragmented using an S220 Focused-ultrasonicator (Covaris). The cDNA library was then amplified using a NEBNext® Ultra™ DNA Library Prep Kit for Illumina (cat. #E7370L, New England Biolabs). Finally, NEBnext library size was estimated using a bioanalyzer with an Agilent High Sensitivity DNA kit. Sequencing was performed using an HiSeq1500 (Illumina) with a single-read sequencing length of 60

bp. TopHat (version 2.1.1; with default parameters) was used to map to the reference genome (UCSC/hg19) with annotation data from iGenomes (Illumina). Levels of gene expression were quantified using Cuffdiff (Cufflinks version 2.2.1; with default parameters).

ATAC-seq and analysis

On day 21 of differentiation, untreated or oxLDL-treated healthy- and WS-iMφs were stained with anti-CD14 and anti-CD11b antibodies, incubated for 30 min on ice, and washed and sorted into 5 × 10^3 CD14$^+$ CD11b$^+$ cells in PBS containing 2% FBS. Library preparation for ATAC-seq was performed on 10,000 cells with a Nextera DNA Sample Preparation kit (cat. #FC-121-1030, Illumina) according to a previously reported protocol [39,40]. Libraries for ATAC were sequenced with a HiSeq 2500 System (Illumina) to generate single-end 50-bp reads. Sequenced single-end reads were mapped to hg19. Duplicate, unmapped or poor-quality reads, mitochondrial reads, and overlaps with the ENCODE blacklist were removed. MACS2 was used to calculate accessible chromatin regions using the options −keep-dup all −nomodel −extsize147 −callsummits −q 0.05. Peaks identified in samples were merged to obtain common genomic coordinates. Peaks with at least 20 CPM in at least one sample were used for further analysis. DARs were calculated between groups of samples using DESeq2. NMF was performed on DARs using the R package "NMF". Motif enrichment in DARs was performed using HOMER.

RTE enrichment analysis

Genomic coordinates of RTEs along with their names, classes, and families were downloaded from the UCSC Genome Browser using the Table Browser with "group" set to "Repeats" and "track" set to "RepeatMasker". Each RTE was assigned reads obtained from the mapped RNA-seq samples within its genomic coordinates. Differentially expressed RTEs between sample groups were calculated using DESeq2.

Detection of total cellular ROS

On day 20 of differentiation, iMφs were serum-starved for 24-36 h and incubated for 6 h with 50 μg/mL DiI-oxLDL. Total cellular ROS was detected in untreated and oxLDL-treated iMφs with the CellROX Deep Red Flow Cytometry Assay Kit (cat. #C10491, Invitrogen) according to the manufacturer's protocol and analyzed with a FACS AriaIII cytometer (BD).

Knock-down assay

Oligonucleotides of shRNA against *IRF3*, *IRF7*, *DHX58*, and *LacZ* (control) were inserted into CS-CDFRfa-EPR lentiviral vector plasmid DNA [42]. The inserted oligonucleotide sequences were as follows:

shCtrl,

CCGGTGTTGGCTTACGGCGGTGATTTCTCGAGAAATCACCGCCGTAAGCCAACTTTTTG

shIRF3_921:

GATCCCCGCCAACCTGGAAGAGGAATTTCTCGAGAAATTCCTCTTCCAGGTTGGCTTTTTGGAAAT

shIRF3_923:
GATCCCCGATCTGATTACCTTCACGGAACTCGAGTTCCGTGAAGGTAATCAGATCTTTTTGGAAAT

shIRF7_859:
GATCCCCGCTGGACGTGACCATCATGTACTCGAGTACATGATGGTCACGTCCAGCTTTTTGGAAAT

shIRF7_862:
GATCCCCCGCAGCGTGAGGGTGTGTCTTCTCGAGAAGACACACCCTCACGCTGCGTTTTTGGAAAT

shDHX58_264:
GATCCCCCTGTTCGATGACCGCAAGAATCTCGAGATTCTTGCGGTCATCGAACAGTTTTTGGAAAT

shDHX58_482:
GATCCCCGCCAGTACCTAGAACTTAAACCTCGAGGTTTAAGTTCTAGGTACTGGCTTTTTGGAAAT

Obtained plasmid DNA was co-transfected with pMD2.G and psPAX2 (both from Addgene) into HEK293T cells using the CalPhos™ Mammalian Transfection Kit (Clontech). HEK293T cells were maintained in IMDM (Gibco) supplemented with 10% fetal calf serum and pen strep L-glutamine (PSG, cat. #10378-016, Gibco). After a medium change with IMDM (10% FBS, PSG, and 1 mM sodium butyrate (B5887, Sigma Aldrich)) on the next day, lentiviruses were concentrated using an Optima L-100 XP ultracentrifuge (Beckman Coulter, rotor type 19, 19000 rpm, 4.5 h, 4°C) and titrated on MOLM-13 AML cell lines.

dsRNA analysis by J2 staining

On day 21 of differentiation, 5×10^4 healthy- and WS-iMφs were washed in PBS and fixed with 4% paraformaldehyde for 10 min at room temperature. Cells were then permeabilized with permeabilization solution (PBS containing 0.1% Triton X-100) for 30 min at room temperature, after which cells were incubated with anti-dsRNA monoclonal antibody J2 (cat. #RNT-SCI-10010200, Jena Bioscience) diluted 1:40 in permeabilization solution for 30 min on ice. Following a wash with permeabilization solution, cells were stained with secondary goat anti-rabbit IgG H&L (cat. #ab150078, Abcam) diluted 1:200 in permeabilization solution for 30 min on ice in the dark. After incubation, cells were washed twice in permeabilization solution and analyzed with a BD FACS Canto II cytometer.

MAVS staining

On day 21 of differentiation, untreated or oxLDL-treated 5×10^4 healthy- and WS-iMφs were washed in PBS and fixed with 4% paraformaldehyde for 10 min at room temperature. Cells were then permeabilized with permeabilization solution for 30 min at room temperature. Cells were resuspended in permeabilization solution, and MAVS monoclonal antibody (ABM28H9) conjugated with APC (cat. #17-

9835-41, eBioscience) was added to the cells followed by 30 min incubation on ice in the dark. After incubation, cells were washed twice in permeabilization solution and analyzed with a BD FACS Canto II cytometer.

Statistical analysis

All analyses were performed with three biological replicates with at least n = 3. Data are shown as mean ± standard error of the mean (SEM). One-way ANOVAs with Bonferroni post hoc tests were performed to determine statistical significance using GraphPad Prism 8 (GraphPad Software, Inc., La Jolla, CA, USA).

Declarations

Data and code availability

Raw and normalized RNA sequences and ATAC data will be deposited in the Bioinformation and DDBJ Center.

Author Contributions

S.K.P. and N.T. designed the study and analyzed the data. S.K.P. carried out the laboratory experiments and created the figures. M.S., Y.M., H.K., Y.O., and N.T. established the iPSCs. S.K.P, M.S., and N.T. established the iPSC-derived Mφs and vascular cells. S.K.P. and N.T. prepared the RNA-seq and ATAC-seq libraries. M.F., B.R., and A.K. sequenced the RNA-seq and ATAC-seq libraries. M. Oshima and N.T. performed the bioinformatic analysis for RNA-seq experiments. A.P. performed the bioinformatic analysis for RTE and ATAC-seq experiments. M. Ohtaka provided the Sendai virus vectors. K.T. generated lentiviruses for knock-down assay. S.K.P and N.T. wrote the manuscript. A.I., K.Y., K.E., and N.T. discussed the data and critically reviewed the manuscript. K.Y., K.E., and N.T. supervised the study. All authors approved the final version of the manuscript.

Conflict of Interest Disclosures

The authors declare that they have no known competing financial interests or personal relationships that could have appeared to influence the work reported in this paper.

References

1.   Mc Namara, K., Alzubaidi, H. & Jackson, J. K. Cardiovascular disease as a leading cause of death: how are pharmacists getting involved? *Integr Pharm Res Pract* **8**, 1–11 (2019).

2.   Brånén Lena *et al.* Inhibition of Tumor Necrosis Factor-α Reduces Atherosclerosis in Apolipoprotein E Knockout Mice. *Arterioscler. Thromb. Vasc. Biol.* **24**, 2137–2142 (2004).

3.   Gareus, R. *et al.* Endothelial cell-specific NF-kappaB inhibition protects mice from atherosclerosis. *Cell Metab.* **8**, 372–383 (2008).

4.   Arango Duque, G. & Descoteaux, A. Macrophage cytokines: involvement in immunity and infectious diseases. *Front. Immunol.* **5**, 491 (2014).

5.   Yu, Q. *et al.* DNA-Damage-Induced Type I Interferon Promotes Senescence and Inhibits Stem Cell Function. *Cell Rep.* **11**, 785–797 (2015).

6.   Baruch, K. *et al.* Aging-induced type I interferon response at the choroid plexus negatively affects brain function. *Science* (2014) doi:10.1126/science.1252945.

7.   Li, Q. *et al.* Interferon regulatory factors IRF5 and IRF7 inhibit growth and induce senescence in immortal Li-Fraumeni fibroblasts. *Mol. Cancer Res.* **6**, 770–784 (2008).

8.   Katlinskaya, Y. V. *et al.* Suppression of Type I Interferon Signaling Overcomes Oncogene-Induced Senescence and Mediates Melanoma Development and Progression. *Cell Rep.* **15**, 171–180 (2016).

9.   Agod, Z. *et al.* Regulation of type I interferon responses by mitochondria-derived reactive oxygen species in plasmacytoid dendritic cells. *Redox Biology* **13**, 633–645 (2017).

10. Studencka-Turski, M., Çetin, G., Junker, H., Ebstein, F. & Krüger, E. Molecular Insight Into the IRE1α-Mediated Type I Interferon Response Induced by Proteasome Impairment in Myeloid Cells of the Brain. *Front. Immunol.* **10**, 2900 (2019).

11. De Cecco, M. *et al.* L1 drives IFN in senescent cells and promotes age-associated inflammation. *Nature* **566**, 73–78 (2019).

12. Sun, S. *et al.* Endogenous retrovirus expression activates type-I interferon signaling in an experimental mouse model of mesothelioma development. *Cancer Lett.* **507**, 26–38 (2021).

13. de Koning, A. P. J., Gu, W., Castoe, T. A., Batzer, M. A. & Pollock, D. D. Repetitive elements may comprise over two-thirds of the human genome. *PLoS Genet.* **7**, e1002384 (2011).

14. Goodier, J. L. Restricting retrotransposons: a review. *Mob. DNA* **7**, 16 (2016).

15. Bulut-Karslioglu, A. *et al.* Suv39h-dependent H3K9me3 marks intact retrotransposons and silences LINE elements in mouse embryonic stem cells. *Mol. Cell* **55**, 277–290 (2014).

16. Huang, C. R. L., Burns, K. H. & Boeke, J. D. Active transposition in genomes. *Annu. Rev. Genet.* **46**, 651–675 (2012).

17. Simon, M. *et al.* LINE1 Derepression in Aged Wild-Type and SIRT6-Deficient Mice Drives Inflammation. *Cell Metab.* **29**, 871–885.e5 (2019).

18. Wang, J. *et al.* Inhibition of activated pericentromeric SINE/Alu repeat transcription in senescent human adult stem cells reinstates self-renewal. *Cell Cycle* **10**, 3016–3030 (2011).

19. Chiappinelli, K. B. *et al.* Inhibiting DNA Methylation Causes an Interferon Response in Cancer via dsRNA Including Endogenous Retroviruses. *Cell* **162**, 974–986 (2015).

20. Leeper, N. J., Hunter, A. L. & Cooke, J. P. Stem cell therapy for vascular regeneration: adult, embryonic, and induced pluripotent stem cells. *Circulation* **122**, 517–526 (2010).

21. Kato, H. *et al.* Generation of disease-specific and CRISPR/Cas9-mediated gene-corrected iPS cells from a patient with adult progeria Werner syndrome. *Stem Cell Res.* **53**, 102360 (2021).

22. Kudlow, B. A., Kennedy, B. K. & Monnat, R. J. Werner and Hutchinson–Gilford progeria syndromes: mechanistic basis of human progeroid diseases. *Nat. Rev. Mol. Cell Biol.* **8**, 394–404 (2007).

23. Goto, M., Ishikawa, Y., Sugimoto, M. & Furuichi, Y. Werner syndrome: a changing pattern of clinical manifestations in Japan (1917\ 2008). *Biosci. Trends* **7**, 13–22 (2013).

24. Huang, S. *et al.* The spectrum of WRN mutations in Werner syndrome patients. *Hum. Mutat.* **27**, 558–567 (2006).

25. Chang, S. *et al.* Essential role of limiting telomeres in the pathogenesis of Werner syndrome. *Nat. Genet.* **36**, 877–882 (2004).

26. Wu, Z. *et al.* Differential stem cell aging kinetics in Hutchinson-Gilford progeria syndrome and Werner syndrome. *Protein Cell* **9**, 333–350 (2018).

27. Laarmann, K., Kress, J. M., Kaina, B. & Fritz, G. Werner syndrome (WRN) DNA helicase and base excision repair (BER) factors maintain endothelial homeostasis. *DNA Repair* **73**, 17–27 (2019).

28. Takayama, N. *et al.* Generation of functional platelets from human embryonic stem cells in vitro via ES-sacs, VEGF-promoted structures that concentrate hematopoietic progenitors. *Blood* **111**, 5298–5306 (2008).

29. Takayama, N. & Eto, K. In vitro generation of megakaryocytes and platelets from human embryonic stem cells and induced pluripotent stem cells. *Methods Mol. Biol.* **788**, 205–217 (2012).

30. Yuzuriha, A. *et al.* Extracellular laminin regulates hematopoietic potential of pluripotent stem cells through integrin β1-ILK-β-catenin-JUN axis. *Stem Cell Res.* **53**, 102287 (2021).

31. Yuzuriha, A. & Eto, K. Revised 'hPSC-Sac Method' for Simple and Efficient Differentiation of Human Pluripotent Stem Cells to Hematopoietic Progenitor Cells. in 1–12 (Springer US).

32. Hirayama, D., Iida, T. & Nakase, H. The Phagocytic Function of Macrophage-Enforcing Innate Immunity and Tissue Homeostasis. *Int. J. Mol. Sci.* **19**, (2017).

33. Noonan, J. *et al.* A Novel Triple-Cell Two-Dimensional Model to Study Immune-Vascular Interplay in Atherosclerosis. *Front. Immunol.* **10**, 849 (2019).

34. Lee, S. J., Baek, S. E., Jang, M. A. & Kim, C. D. SIRT1 inhibits monocyte adhesion to the vascular endothelium by suppressing Mac-1 expression on monocytes. *Exp. Mol. Med.* **51**, 1–12 (2019).

35. Bennett, M. R., Sinha, S. & Owens, G. K. Vascular Smooth Muscle Cells in Atherosclerosis. *Circ. Res.* **118**, 692–702 (2016).

36. Alexander, M. R. & Owens, G. K. Epigenetic control of smooth muscle cell differentiation and phenotypic switching in vascular development and disease. *Annu. Rev. Physiol.* **74**, 13–40 (2012).

37. Linker, R. A. *et al.* Fumaric acid esters exert neuroprotective effects in neuroinflammation via activation of the Nrf2 antioxidant pathway. *Brain* **134**, 678–692 (2011).

38. Vomund, S., Schäfer, A., Parnham, M. J., Brüne, B. & von Knethen, A. Nrf2, the Master Regulator of Anti-Oxidative Responses. *Int. J. Mol. Sci.* **18**, (2017).

39. Buenrostro, J. D., Giresi, P. G., Zaba, L. C., Chang, H. Y. & Greenleaf, W. J. Transposition of native chromatin for fast and sensitive epigenomic profiling of open chromatin, DNA-binding proteins and nucleosome position. *Nat. Methods* **10**, 1213–1218 (2013).

40. Takayama, N. *et al.* The Transition from Quiescent to Activated States in Human Hematopoietic Stem Cells Is Governed by Dynamic 3D Genome Reorganization. *Cell Stem Cell* **28**, 488–501.e10 (2021).

41. Wang, J. *et al.* ATAC-Seq analysis reveals a widespread decrease of chromatin accessibility in age-related macular degeneration. *Nat. Commun.* **9**, 1364 (2018).

42. Sone, M. *et al.* Silencing of p53 and CDKN1A establishes sustainable immortalized megakaryocyte progenitor cells from human iPSCs. *Stem Cell Reports* (2021) doi:10.1016/j.stemcr.2021.11.001.

43. Sakellariou, G. K. *et al.* Studies of mitochondrial and nonmitochondrial sources implicate nicotinamide adenine dinucleotide phosphate oxidase(s) in the increased skeletal muscle superoxide generation that occurs during contractile activity. *Antioxid. Redox Signal.* **18**, 603–621 (2013).

44. Decout, A., Katz, J. D., Venkatraman, S. & Ablasser, A. The cGAS−STING pathway as a therapeutic target in inflammatory diseases. *Nat. Rev. Immunol.* **21**, 548−569 (2021).

45. Cantarella, S. *et al.* Alu RNA Modulates the Expression of Cell Cycle Genes in Human Fibroblasts. *Int. J. Mol. Sci.* **20**, (2019).

46. Colombo, A. R., Triche, T., Jr & Ramsingh, G. Transposable Element Expression in Acute Myeloid Leukemia Transcriptome and Prognosis. *Sci. Rep.* **8**, 16449 (2018).

47. Ohms, S. & Rangasamy, D. Silencing of LINE-1 retrotransposons contributes to variation in small noncoding RNA expression in human cancer cells. *Oncotarget* **5**, 4103−4117 (2014).

48. Bogu, G. K., Reverter, F., Marti-Renom, M. A., Snyder, M. P. & Guigó, R. Atlas of transcriptionally active transposable elements in human adult tissues. *bioRxiv* 714212 (2019) doi:10.1101/714212.

49. Senapati, P. *et al.* Aging leads to stochastic loss of silencing at transposons in mammary luminal epithelial cells. *bioRxiv* 2020−2006 (2020).

50. Onomoto, K., Onoguchi, K. & Yoneyama, M. Regulation of RIG-I-like receptor-mediated signaling: interaction between host and viral factors. *Cell. Mol. Immunol.* **18**, 539−555 (2021).

51. Roulois, D. *et al.* DNA-Demethylating Agents Target Colorectal Cancer Cells by Inducing Viral Mimicry by Endogenous Transcripts. *Cell* **162**, 961−973 (2015).

52. Gorbunova, V. *et al.* The role of retrotransposable elements in ageing and age-associated diseases. *Nature* **596**, 43−53 (2021).

53. Lin, J.-Y., Kuo, R.-L. & Huang, H.-I. Activation of type I interferon antiviral response in human neural stem cells. *Stem Cell Res. Ther.* **10**, 387 (2019).

54. Kumagai, Y. *et al.* Cutting Edge: TLR-Dependent viral recognition along with type I IFN positive feedback signaling masks the requirement of viral replication for IFN-{alpha} production in plasmacytoid dendritic cells. *J. Immunol.* **182**, 3960−3964 (2009).

55. Hobeika, A. C., Subramaniam, P. S. & Johnson, H. M. IFNα induces the expression of the cyclin-dependent kinase inhibitor p21 in human prostate cancer cells. *Oncogene* **14**, 1165−1170 (1997).

56. Besch, R. *et al.* Proapoptotic signaling induced by RIG-I and MDA-5 results in type I interferon-independent apoptosis in human melanoma cells. *J. Clin. Invest.* **119**, 2399−2411 (2009).

57. Yu, Q. *et al.* Type I interferon controls propagation of long interspersed element-1. *J. Biol. Chem.* **290**, 10191−10199 (2015).

58. Cuellar, T. L. *et al.* Silencing of retrotransposons by SETDB1 inhibits the interferon response in acute myeloid leukemia. *J. Cell Biol.* **216**, 3535−3549 (2017).

59. Sone, M. *et al.* Different differentiation kinetics of vascular progenitor cells in primate and mouse embryonic stem cells. *Circulation* **107**, 2085–2088 (2003).

60. Sone, M. *et al.* Pathway for differentiation of human embryonic stem cells to vascular cell components and their potential for vascular regeneration. *Arterioscler. Thromb. Vasc. Biol.* **27**, 2127–2134 (2007).
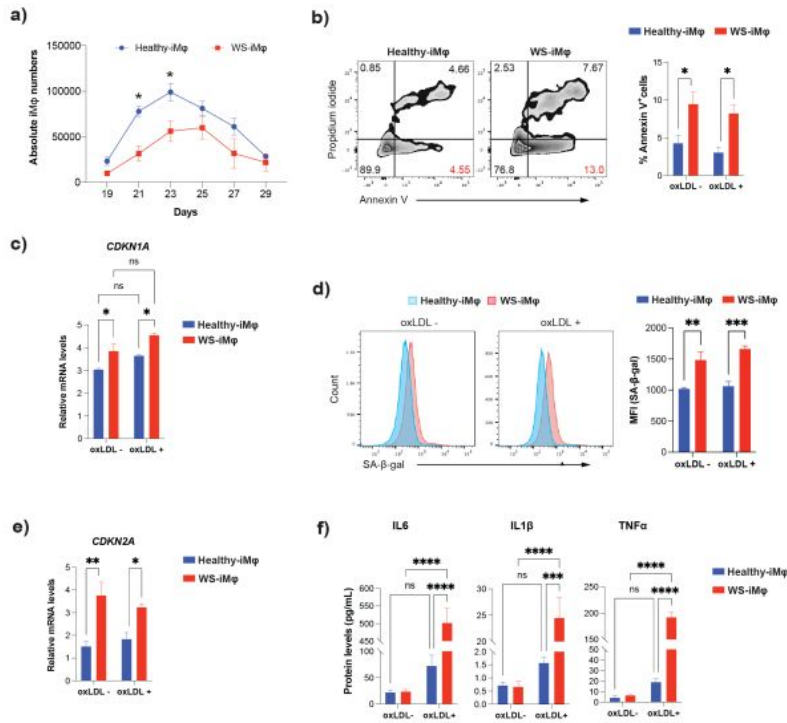
Figures

Figure 1

Figure 1

Apoptosis and cellular senescence lead to impaired WS-iMφ proliferation. a) Absolute numbers of CD14^{+} CD11b^{+} healthy- and WS-iMφs. **b)** Representative flow cytometric plots of annexin V staining in healthy- and WS-iMφs without oxLDL treatment (left) and proportion of annexin V^{+} cells among healthy- and WS-iMφs before and after oxLDL treatment (right). **c)** mRNA levels of *CDKN1A* normalized by *GAPDH* mRNA.

d) Representative flow cytometric plots of SA-β-gal staining (left) and SA-β-gal MFI (right) between healthy- and WS-iMφs before and after oxLDL treatment. **e)** mRNA levels of *CDKN2A* normalized by GAPDH mRNA. **f)** Secreted pro-inflammatory cytokine protein levels for healthy- and WS-iMφs before and after oxLDL treatment. Data are shown as the mean ± standard error of the mean (SEM) of three independent experiments. *p < 0.05, **p < 0.01, ***p < 0.001, ****p < 0.0001. ns, not significant.

Figure 2

Figure 2
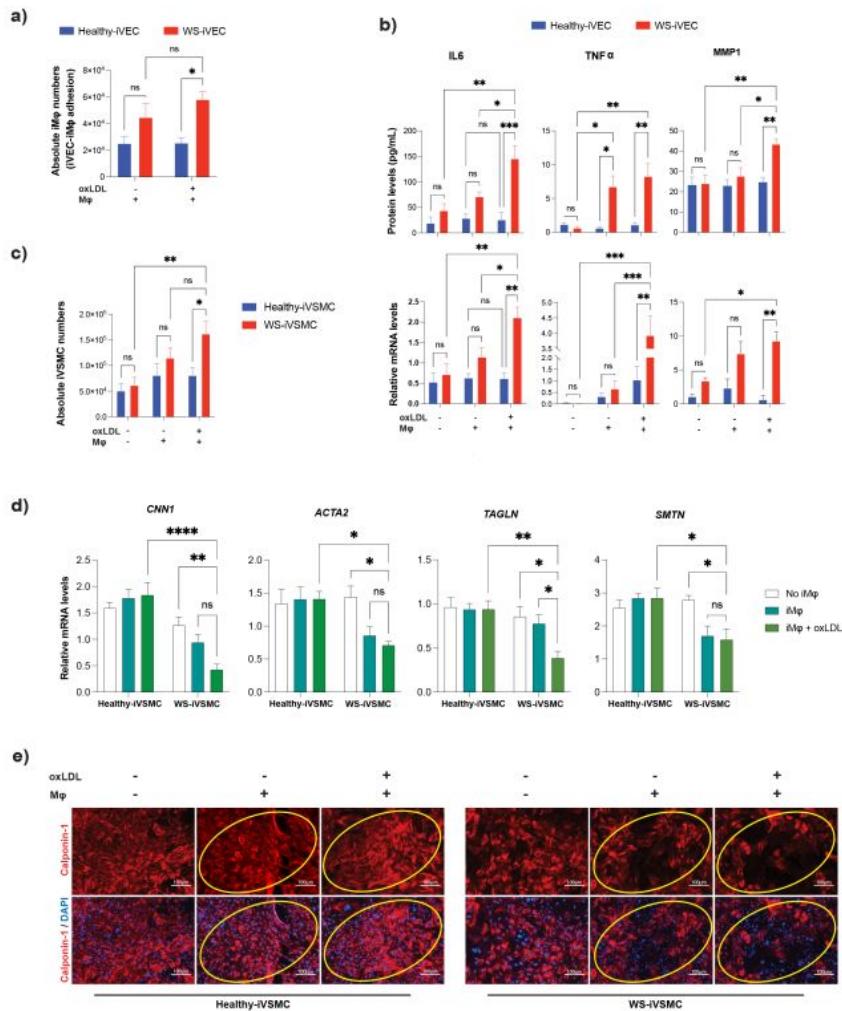
Effects of inflammatory iMφs on iPSC-derived vascular cells. a) Absolute numbers of CD14^{+} adherent iMφs on iVECs after co-culture. **b)** IL6, TNFα, and matrix metalloproteinase-1 (MMP1) protein levels (top) and mRNA levels normalized by *GAPDH* mRNA (bottom) before and after co-culture with untreated or oxLDL-treated Mφs. **c)** Absolute numbers of healthy- and WS-iVSMCs before and after co-culture with untreated or oxLDL-treated Mφs. **d)** mRNA levels of VSMC contractile markers normalized by *GAPDH* mRNA before and after co-culture with untreated or oxLDL-treated Mφs. **e)** Immunocytochemistry of calponin-1 protein in healthy- and WS-iVSMCs before and after co-culture with untreated or oxLDL-treated Mφs. Data are shown as the mean ± SEM of three independent experiments.*p < 0.05, **p < 0.01, ***p < 0.001, ****p < 0.0001. ns, not significant.

Figure 3

RNA-seq analysis in healthy- and WS-iMφs. a) Schematic diagram of RNA-seq library preparation. **b)** Heatmap of differentially expressed genes in healthy- and WS-iMφs before and after oxLDL treatment. Differentially expressed genes were obtained from Cuffdiff and grouped into four clusters by K-means clustering, with each column representing a sample group and each row representing an individual gene. **c)** Cluster-wise representation of differentially expressed genes in each group. **d)** Pathway enrichment analysis in each cluster. The yellow line represents the threshold for statistical significance. **e)** Heatmap of vital cell cycle regulators and DNA repair-related genes. **f)** Pathway enrichment analysis in each cluster. The yellow line represents the threshold for statistical significance. **g)** Heatmap of type I IFN signature gene sets in untreated and oxLDL-treated healthy- and WS-iMφs. **h)** Heatmap of apoptotic cell clearance gene sets in untreated and oxLDL-treated healthy- and WS-iMφs. Data are shown as z-scores calculated from fragments per kilobase of exon per million reads mapped (FPKM) values.
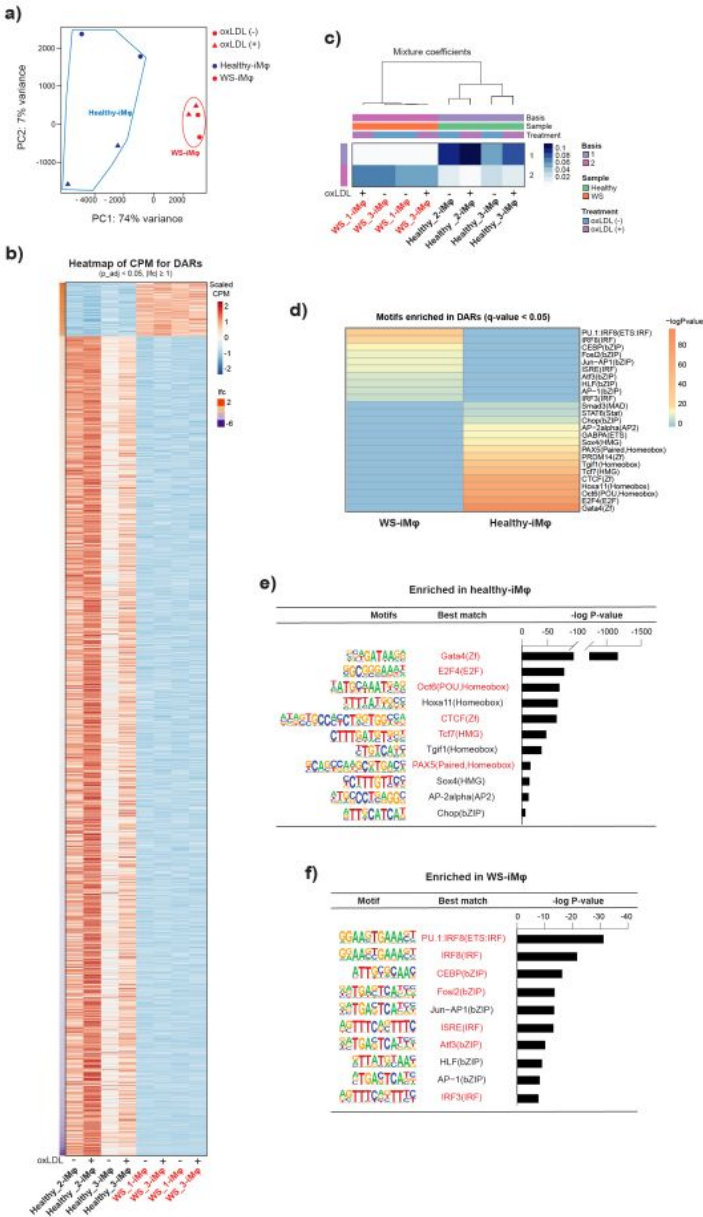
Figure 4

Type I IFN-specific chromatin accessibility profile in WS-iMφs. a) Principal component analysis of untreated and oxLDL-treated healthy- and WS-iMφs. **b)** Heatmap of counts per million (CPM) of differentially accessible regions (DARs) calculated using DESeq2 in healthy- and WS-iMφs, with each column representing the CPM of each DAR within a sample and each row representing an individual DAR. **c)** Heatmap showing NMF mixture coefficients for each basis within the samples. **d)** Heatmap showing

enriched motifs in DARs in healthy- and WS-iMφs. **e)** HOMER motif enrichment analysis in healthy-iMφs. **f)** HOMER motif enrichment analysis in WS-iMφs.

Figure 5

Type I IFN signal-dependent cellular senescence and inflammation in WS-iMφs. a) Percent knock-down (KD) efficiency by shIRF3 and shIRF7. **b)** mRNA levels of type I IFN signature genes normalized by *GAPDH* mRNA after lentiviral transduction of shIRF3 and shIRF7. **c)** Fold change in absolute numbers of WS-iMφs after lentiviral transduction of shIRF3 and shIRF7. **d)** Representative flow cytometric plots of SA-β-gal staining (left) and MFI (right) after lentiviral transduction of shIRF3 and shIRF7. **e)** *CDKN2A* mRNA levels normalized by *GAPDH* mRNA. **f)** Pro-inflammatory cytokine levels after lentiviral transduction of shIRF3 and shIRF7. **g)** *IL6* and *TNFα* mRNA levels normalized by *GAPDH* mRNA after lentiviral transduction of shIRF3 and shIRF7. Data are shown as mean ± SEM of three independent experiments. *p < 0.05, **p < 0.01, ***p < 0.001, ****p < 0.0001.

Figure 6

Activation of RTEs triggers innate immunity in WS-iMφs. a) Heatmaps showing differential expression of RTEs obtained using DESeq2 in healthy- and WS-iMφs (left) before and after oxLDL treatment and in healthy aged-PB-Mφs and WS-PB-Mφs (right), with each column representing a sample group and each row representing an individual RTE. **b)** Numbers of individual RTEs at sub-family (LINE, SINE, and ERV) level in untreated healthy- and WS-iMφs. **c)** Numbers of individual RTEs at sub-family level in healthy- and WS-iMφs treated with oxLDL. **d)** Numbers of individual RTEs at sub-family level in healthy aged-PB-Mφs and WS-PB-Mφs. **e)** Venn diagram showing commonly upregulated RTEs between WS-iMφs and WS-PB-Mφs as defined by a statistically significant (adjusted p-value ≤ 0.05) 2-fold change in normalized expression between healthy and WS samples. **f)** Expression levels of significantly enriched individual members of the LINE sub-family. **g)** Expression levels of significantly enriched individual members of the SINE sub-family. **h)** Expression levels of significantly enriched individual members of the ERV sub-family. Expression levels were derived from CPM values, and p-values were obtained from t-tests.

Figure 7

DHX58-dependent dsRNA sensing pathway initiates transcription of type I IFN signature genes. a) Schematic diagram of *DHX58*-dependent dsRNA sensing pathway. **b)** Representative fluorescence-activated cell sorting (FACS) plot of dsRNA accumulation (left) and MFI of dsRNA accumulation (right) in healthy- and WS-iMφs. **c)** Representative FACS plot of MAVS expression (left) and MFI of MAVS expression (right) in healthy- and WS-iMφs. **d)** Percent knock-down efficiency of lentiviral transduction of shDHX58. **e)** mRNA levels of type I IFN signature genes normalized by *GAPDH* mRNA after lentiviral transduction with shDHX58. Data are shown as the mean ± SEM of three independent experiments. *p < 0.05, **p < 0.01, ***p < 0.001, ****p < 0.0001.

Supplementary Files

This is a list of supplementary files associated with this preprint. Click to download.

- extendeddata.pdf
- ExtendedDataLegends.docx